Nano Research

Open Access

Research Article

Magnetically actuated aggregation of nanoparticles via host–guest interaction for extracellular targeted drug delivery and cancer immunotherapy

Fangzheng Li[1,§], Yueqiang Zhu[1,§], Dongli Qi[1], Chaoran Chen[1], Hao Li[1], Ziyang Cao[2] ✉, and Xianzhu Yang[1,3] ✉

[1] *School of Biomedical Sciences and Engineering, South China University of Technology, Guangzhou International Campus, Guangzhou 511442, China*
[2] *Department of General Surgery, Guangzhou First People's Hospital, the Second Affiliated Hospital, School of Medicine, South China University of Technology, Guangzhou 510180, China*
[3] *National Engineering Research Center for Tissue Restoration and Reconstruction, and Guangdong Province Key Laboratory of Biomedical Engineering, South China University of Technology, Guangzhou 510006, China*
§ *Fangzheng Li and Yueqiang Zhu contributed equally to this work.*

Cite this article: *Nano Research*, **2025**, *18*, 94907164. https://doi.org/10.26599/NR.2025.94907164

ABSTRACT: Rational design of nanomedicine can efficiently improve the therapeutic activity of anticancer drugs; however, the current design strategies are to increase the concentration of drugs within targeted cells, which is not applicable to extracellular-targeted drugs. Herein, we report a nanoparticular aggregation strategy via magnetic actuation and host–guest interaction for extracellular drug delivery. The β-cyclodextrin (βCD)-decorated magnetic nanoparticles (βCD-MNPs) were first administrated and infiltrated into tumor tissue under the magnetic actuation, and then generated mild hyperthermia under alternating magnetic field (AMF) to improve the infiltration of another adamantane (Ad)-decorated NPs (Ad-NPs) into the tumor tissue. Subsequently, the βCD-MNP and Ad-NP would form micro-sized aggregation via the host–guest interaction, which could significantly enhance the enrichment and retention of extracellular-targeted drugs and also minimize their cellular uptake. This nanoparticular aggregation strategy remarkably improved the therapeutic activity of batimastat and PD-1/PD-L1 inhibitor 1 (BMS-1), both of which were extracellular-targeted drug. Such nanoparticular aggregation strategy represents a rational avenue for extracellular drug delivery.

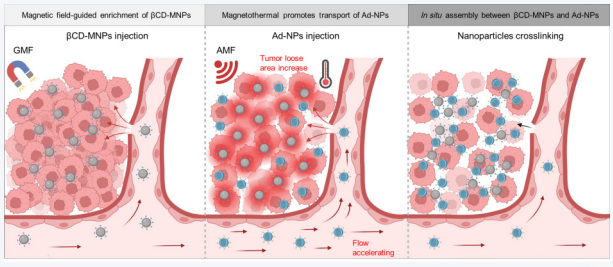

KEYWORDS: nanoparticular aggregation, magnetic actuation, host–guest interaction, extracellular targeted drugs, programmed death protein 1 (PD-1)/programmed cell death ligand 1 (PD-L1) blockage

1 Introduction

Nanoparticle (NP)-based drug delivery systems have been widely developed, and hundreds of NP-based drugs have been clinically approved for various diseases treatment, especially in cancer therapy [1–6]. More recently, numerous tumor microenvironment-responsive drug delivery systems including charge conversion [7–9], size shrinkage [10–12], stimuli-responsive release [13–15], and so on [16], have been explored to improve the delivery efficiency in blood circulation, tumor accumulation, penetration, cellular uptake, and intracellular release [17–20]. Ultimately, these strategies could efficiently elevate the intracellular concentration of therapeutic agents and consequently achieve better anticancer efficacy. This design principle is derived from the fact that drug delivery systems were originally developed mainly for the delivery of small molecule chemotherapy drugs [21–23].

With the continuous emergence of new cancer treatment drugs, previous design principles of delivery systems can no longer meet the needs [24–26]. For instance, the matrix metalloproteinase (MMP) inhibitors [27–29], which were employed to suppress the activity of MMP to inhibit tumor metastasis, should be retained in the extracellular space rather than in tumor cells, because these MMP functioned in the extracellular environment and degrade matrix to facilitate tumor cells metastasis [30, 31]. In addition, the

Received: September 28, 2024; **Revised:** November 22, 2024
Accepted: November 29, 2024

✉Address correspondence to Ziyang Cao, mccaozy@scut.edu.cn; Xianzhu Yang, yangxz@scut.edu.cn

delivery systems of antibodies should minimize the cellular uptake after accumulating into tumor tissue since their corresponding receptors locate in the cell membrane [32, 33]. Thus, previous design principles were difficult to meet the needs of these extracellular-targeted drugs, and it is highly desired to develop the delivery system of extracellular and membrane-targeted drug [34–36].

Taken these in mind, we report a nanoparticular aggregation strategy via magnetic actuation and host–guest interaction for the delivery of extracellular-targeted drug (Fig. 1). The β-cyclodextrin (βCD)-decorated Fe_3O_4 magnetic NPs (βCD-MNPs) were first administrated and infiltrated into tumor tissue under the magnetic actuation [37, 38], and then generated mild hyperthermia under alternating magnetic field (AMF) to improve nanoparticle penetration into the tumor deeper regions. Subsequently, another nanoparticles, Ad-NPs, were intravenously injected and then assemble with the pre-administrated βCD-MNPs to form aggregation via the host–guest interaction, which could significantly enhance the retention and accumulation of Ad-NPs and also minimize the cellular uptake. This nanoparticular aggregation strategy efficiently improved the therapeutic activity of batimastat (a small molecule inhibitor of extracellular MMP) and BMS-1 (a small molecule inhibitor of membrane programmed death protein 1 (PD-1)/programmed cell death ligand 1 (PD-L1), both of which were extracellular-targeted drug.

2 Results and discussion

To achieve the nanoparticular aggregation, the βCD-MNPs were first synthesized according to the previously reported method [39, 40]. The dynamic light scattering (DLS) and atomic force microscopy (AFM) analysis demonstrated that the obtained βCD-MNPs had a spherical shape with a particle size of approximately 105 nm (Figs. 2(a) and 2(b)). And, the weight ratio of β-CD in βCD-MNPs was 12.04% according to the thermogravimetric analysis compared to that of Fe_3O_4 (Fig. S1 in the Electronic Supplementary Material (ESM)). Subsequently, the adamantane-terminal amphiphilic copolymer poly(ethylene glycol)-*b*-polylactide (Ad-PEG-*b*-PLA) was synthesized (Fig. S2 in the ESM) and used to prepare the polymeric nanoparticles Ad-NPs through the nanoprecipitation method. The size of Ad-NPs was approximately 90 nm (Figs. 2(c) and 2(d)). And, both βCD-MNPs and Ad-NPs displayed excellent colloidal stability in fetal bovine serum (FBS) within 48 h (Fig. S3 in the ESM).

According to our design, the host–guest interaction between the βCD moiety of βCD-MNPs and Ad moiety of Ad-NPs would lead to aggregation of NPs (denoted as Agg-NPs). Isothermal titration calorimetry (ITC) analysis displayed a significant exothermic peak during the titration of Ad-NPs into βCD-MNPs with the binding constant (K_D) is 6.182 μM (Fig. 2(e) and Fig. S4(a) in the ESM), which was not observed in the control group. Morever, the K_D value between Ad-NPs into βCD-MNPs is significantly lower than that of free Ad/βCD (15.42 μM, Fig. S4(b) in the ESM), which could be attributed to the nanoparticles offering multiple binding sites on the surface, resulting in acquired stronger binding affinity. Furthermore, we attached Ad-NPs or NPs to atomic force microscopy (AFM) cantilevers, and βCD-MNPs were placed on a slide to measure their interaction force (Fig. 2(f)). AFM measurement demonstrated that the interaction force between βCD-MNPs and Ad-NPs was approximately 14 nN but negligible between βCD-MNPs and NPs, indicating their strong host–guest interaction. Apparently, when the βCD-MNPs and Ad-NPs were mixed, aggregates with an average size of 1200 nm could be found within 1.0 min, and numerous black aggregates were observed at the bottom (Fig. 2(g)). In contrast, no aggregation was observed in the mixture of the βCD-MNPs and NPs of PEG-*b*-PLA without Ad decoration. The AFM analysis similarly revealed the formation of numerous particle aggregates in the Agg-NPs solution, whereas the

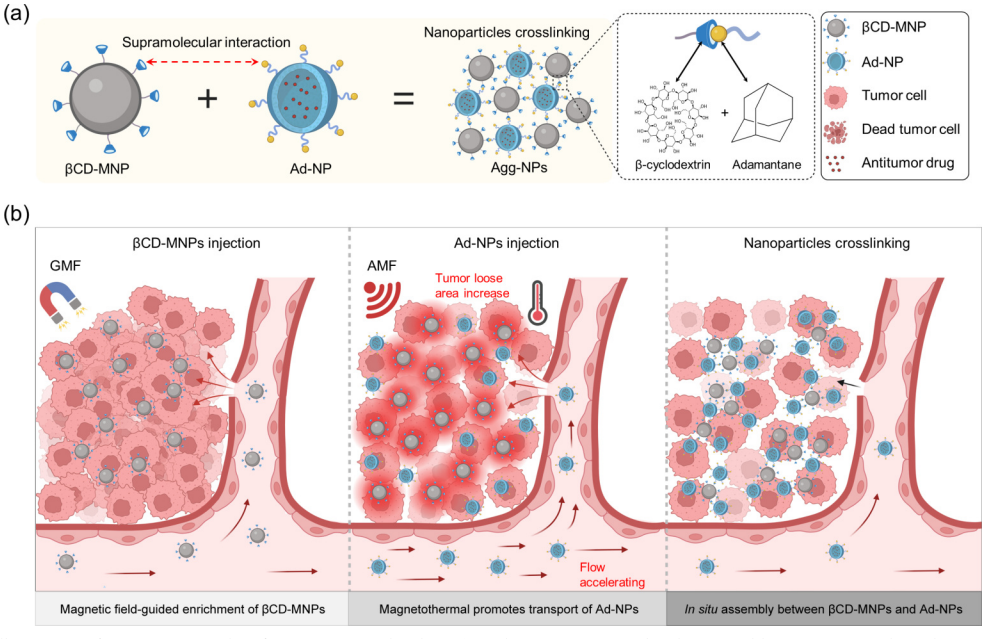

Figure 1 Schematic illustrating of two nanoparticles (βCD-MNPs and Ad-NPs) undergoing supramolecular assembly to construct drug depots within tumor area. (a) The Ad-NPs and βCD-MNPs occurred host–guest interaction and formed micro-size aggregation. (b) βCD-MNPs are first effectively enriched at the tumor site under magnetic field guidance (+M). Subsequently, an alternating magnetic field (+AMF) is applied to the tumor tissue with generating magnetothermal effects that enhance blood flow and loosen the tumor structure resulted in facilitating the accumulation of Ad-NPs at the tumor site. Ultimately, βCD-MNPs and Ad-NPs undergo *in situ* supramolecular assembly within the tumor to form micro-size nanoparticle aggregation (Agg-NPs).

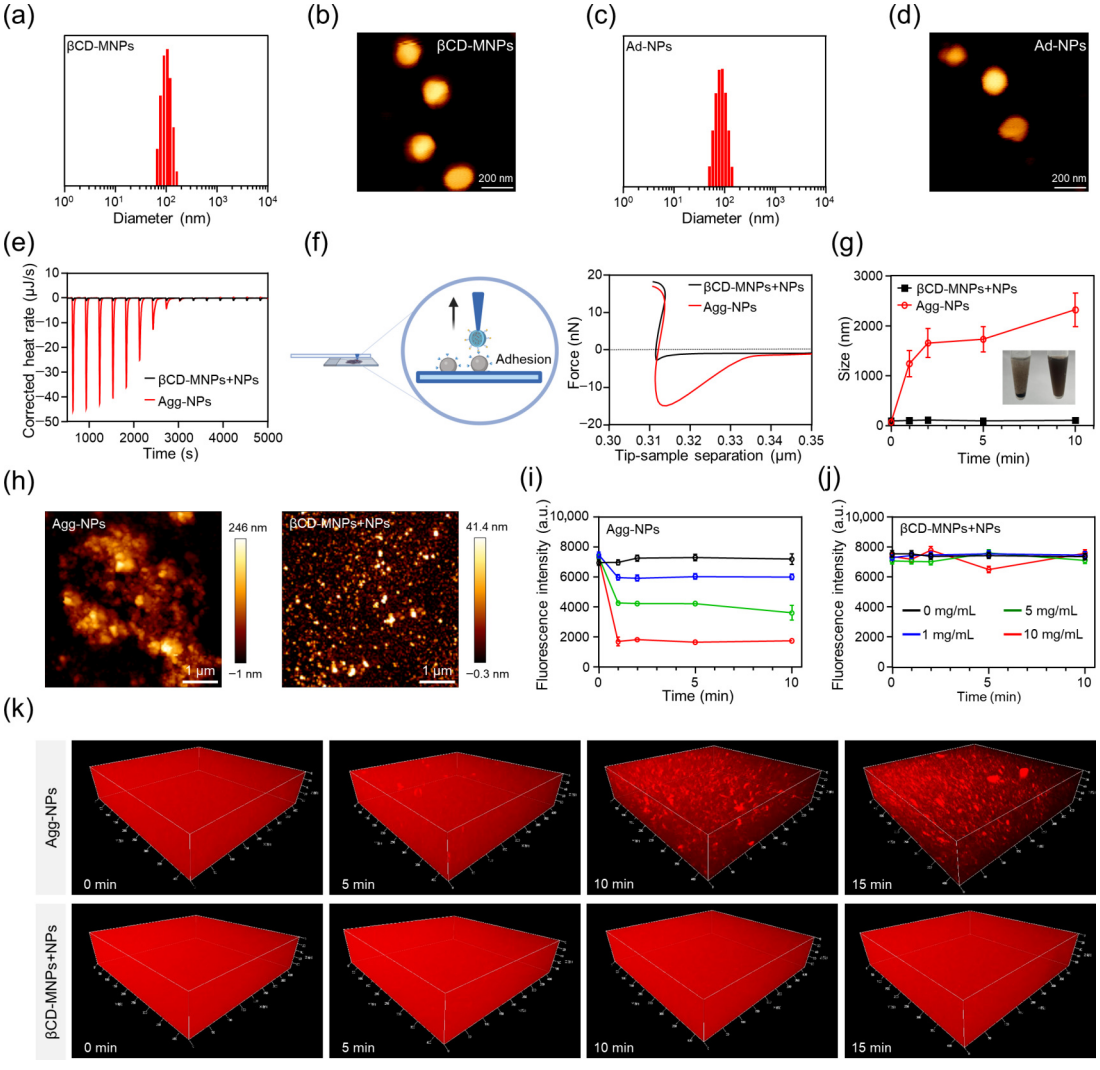

Figure 2 (a) Average hydrodynamic size and (b) representative morphology image of βCD-MNPs measured by DLS and AFM, respectively. Scale bar, 200 nm. (c) Average hydrodynamic size and (d) representative morphology image of Ad-NPs measured by DLS and AFM, respectively. Scale bar, 200 nm. (e) ITC measurement of Agg-NPs or βCD-MNPs+NPs. (f) Supramolecular interaction force between Ad-NPs and βCD-MNPs measured by AFM. (g) DLS measurements of the hydrodynamic diameters of Agg-NPs or βCD-MNPs+NPs after co-incubation. (h) Representative AFM image of Agg-NPs and βCD-MNPs+NPs. The fluorescence intensity in the supernatant of mixed solution of Agg-NPs (i) or βCD-MNPs+NPs (j) after centrifugation with different concentrations of βCD-MNPs. (k) 3D CLSM images of the Agg-NPs or βCD-MNPs+NPs aqueous solutions after co-incubation for various lengths of time. The Ad-NPs (0.1 mg/mL) or NPs (0.1 mg/mL) was labeled with DiD and the concentration of βCD-MNPs was fixed in 0.1 mg/mL.

βCD-MNPs+NPs group did not exhibit such prominent particle aggregation (Fig. 2(h)). In addition, after co-incubation of DiD-labeled Ad-NPs with various concentrations of βCD-MNPs, the formed aggregates were separated using a magnet, and the fluorescence intensity of unaggregated Ad-NPs in the supernatant was measured. It could be found that unaggregated Ad-NPs in the supernatant decreased with the increase of βCD-MNPs (Figs. 2(i)), while the fluorescence intensity of NPs in the supernatant was not changed after the addition of βCD-MNPs (Fig. 2(j)).

Furthermore, to intuitively monitor the nanoparticular aggregation, we used confocal laser scanning microscopy (CLSM) to observe the DiD-labeled Ad-NPs and βCD-MNPs. Obviously, micro-size aggregates rapidly emerged, and their size increased with increasing co-incubation time (Fig. 2(k)), which was not found in the mixture of NPs and βCD-MNPs. And, the formed Agg-NPs were dependent on the concentration of βCD-MNPs (Fig. S5 in the ESM). Interestingly, Ad-NPs and βCD-MNPs aggregate into large particles will decrease uptake and endocytosis by tumor cells (Fig. S6 in the ESM). Besides, Ad-NPs and βCD-MNPs exhibited great biocompatibility (Fig. S7 in the ESM). Collectively, these results demonstrated the host–guest interaction of βCD moiety of βCD-MNPs and Ad moiety of Ad-NPs induced the rapid formation of micro-size aggregates Agg-NPs.

To investigate whether Agg-NPs would be formed *in vivo*, orthotopic 4T1 tumor-bearing mice were intravenously (i.v.) administered of βCD-MNPs and followed by DiD-labeled Ad-NPs or NPs, and then monitored using a fluorescence *in vivo* imaging system (IVIS). It could be found that mice administrated of Agg-NPs exhibited much enhanced fluorescence signals in tumor tissue compared to that of βCD-MNPs+NPs group (Figs. 3(a) and 3(b)). In addition, when a magnet was placed in the tumor regions to improve the accumulation of βCD-MNPs, the fluorescence signals of DiD-labeled Ad-NPs were further increased (Agg-NPs(+M) group). More interesting, applying the AMF to generate more

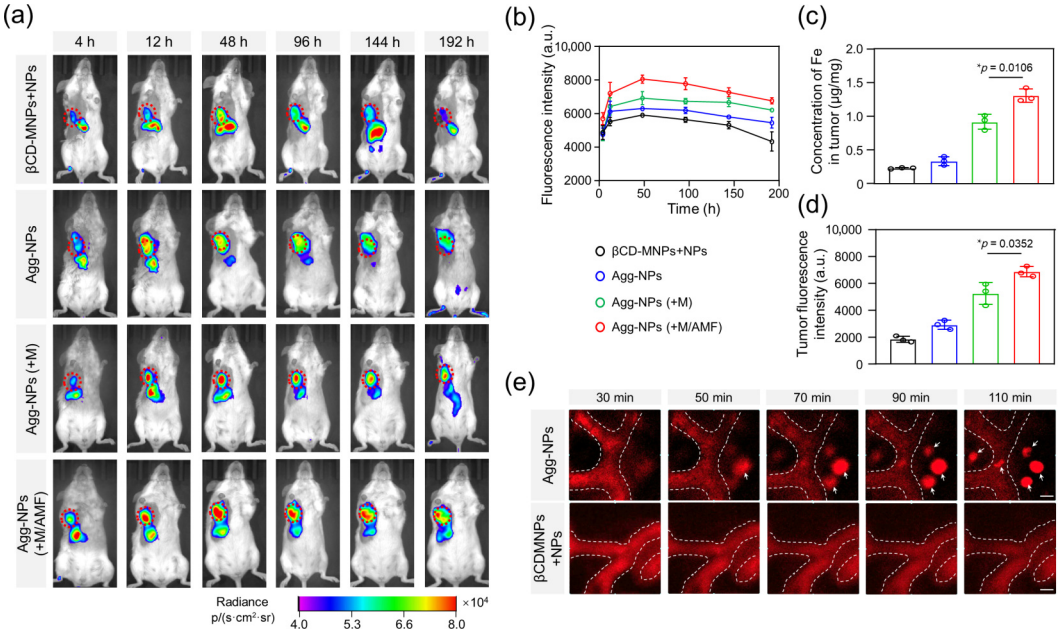

Figure 3 (a) IVIS imaging of 4T1 tumor-bearing mice at different times after i.v. injection of βCD-MNPs and subsequent NP_{DiD} or Ad-NP_{DiD} administration (n = 3). Red circles indicated tumor sites. (b) The change curves of fluorescence in tumor site after administration of various formulations. Data are presented as the mean ± s.d. (n = 3). (c) The contents of Fe in tumor tissues measured by ICP-MS and (d) DiD fluorescence intensity statistic in tumor tissues at the 192 h post-administration in (a). Data are presented as the mean ± s.d. (n = 3). (e) Intravital CLSM real-time visualization of Agg-NPs or βCD-MNPs+NPs in 4T1 tumor-bearing mice. Both Ad-NPs and NPs were labeled with DiD. Scale bar, 20 μm.

heating based on aggregation effect (Fig. S8 in the ESM), the fluorescence signals in tumor regions (Agg-NPs(+M/AMF) group) reached highest among these formulations and could be clearly detected even 192 h post injection. And, this nanoparticular aggregation-mediated tumor enrichment and long-term retention were further verified by the measuring of the contents of Fe and DiD in the tumor tissue (Figs. 3(c) and 3(d)). To investigate why the magnetothermal treatment can further enhance tumor enrichment and retention of Agg-NPs, we employed the previous reported method to determine the tumor tissue [41–45]. It could be found that the percentage of loose tumor tissue after applying AMF treatment increased from 4.2% to 32.8% (Fig. S9(a) in the ESM). In addition, the small animal ultrasound revealed that the blood flow velocity around the tumor was significantly increased after mild hyperthermia treatment (Figs. S9(b) and S9(c) in the ESM).

Furthermore, we used intravital CLSM to visualize the formation of Agg-NPs in the tumor in real time. Mice bearing an orthotopic 4T1 tumor with ear window chambers were i.v. injected βCD-MNPs and subsequently i.v. injected DiD-labeled Ad-NPs or the control formulation NPs, and then the assembly process was observed by intravital CLSM. As shown in Fig. 3(e) and Movies S1 and S2 in the ESM, the red fluorescence aggregates were observed in the tumor site at 50 min post-injection in the Agg-NPs group, which was not the case in the mice treated with βCD-MNPs+NPs group. These results suggested that Agg-NPs can achieve the formation of micro-sized particle aggregates *in vivo* at the tumor site.

Furthermore, to evaluate the enhanced therapeutic efficacy of the Agg-NPs delivery strategy, batimastat (BB94) [46], which is an effective broad-spectrum extracellular MMP inhibitor, was selected as a model drug and encapsulated in the Ad-NPs or NPs. Then, mice bearing 4T1 tumor were randomly divided into seven groups (n = 5) (Fig. 4(a)): G1: PBS, G2: free BB94, G3: NP_{BB94}/βCD-MNPs(+M), G4: NP_{BB94}/βCD-MNPs(+M/AMF), G5: Agg-NP_{BB94}, G6: Agg-NP_{BB94}(+M), and G7: Agg-NP_{BB94}(+M/AMF). βCD-MNPs were intravenously injected in groups G3–G7; (+M) represented fixing a magnet at the tumor site in groups G3, G4, G6, and G7 for 15 min, and (+M/AMF) represented further applying AMF treatment to heat the tumor to 39–41 °C for 10 min.

Ad-NP_{BB94} or NP_{BB94} was intravenously injected at a BB94 dosage of 5.0 mg/kg body weight. Lung and tumor tissues were collected at day 27 to evaluate the inhibition efficacy of tumor metastasis and growth. As shown in Figs. 4(b) and 4(c), mice treated with NP_{BB94}/βCD-MNPs(+M) or NP_{BB94}/βCD-MNPs(+M/AMF) slightly decreased lung metastasis inhibition, exhibiting a 31.0% and 44.1% reduction, respectively. In contrast, treatment with the Agg-NP_{BB94}, Agg-NP_{BB94}(+M), or Agg-NP_{BB94}(+M/AMF) exhibited significantly enhanced inhibition efficacies of lung metastasis, especially Agg-NP_{BB94}(+M/AMF) with a 78.7% reduction. Moreover, Agg-NP_{BB94}(+M/AMF) treatment also exhibited the highest efficacy to suppress the primary tumor growth (Fig. 4(d) and Fig. S10 in the ESM), which should attribute to remarkably improved tumor enrichment and long-term retention via nanoparticular aggregation (Fig. 3). Notably, the expression of MMP-3 and MMP-9 was strikingly declined in the Agg-NP_{BB94}(+M/AMF) group (Figs. 4(e) and 4(f) and Fig. S11 in the ESM). In addition, Agg-NP_{BB94}(+M/AMF) treatment displayed good biosafety via monitoring the body weight changes (Fig. S12 in the ESM) and biochemical analysis (Fig. S13 in the ESM).

It is well-known that malignant tumor cells usually overexpressed the PD-L1 to bind PD-1 of T cells, which induced the immune evasion of tumors. And, PD-1/PD-L1 based pathway is an important immune checkpoint in cancer immunotherapy. Thus, the small molecule inhibitor BMS-1 [47, 48], which extracellularly disturbed the interaction between PD-1 and PD-L1, was chosen to evaluate the efficacy of this nanoparticular aggregation strategy. We encapsulated the BMS-1 into Ad-NPs or NPs using nanoprecipitation method. Mice bearing B16-F10 tumor were

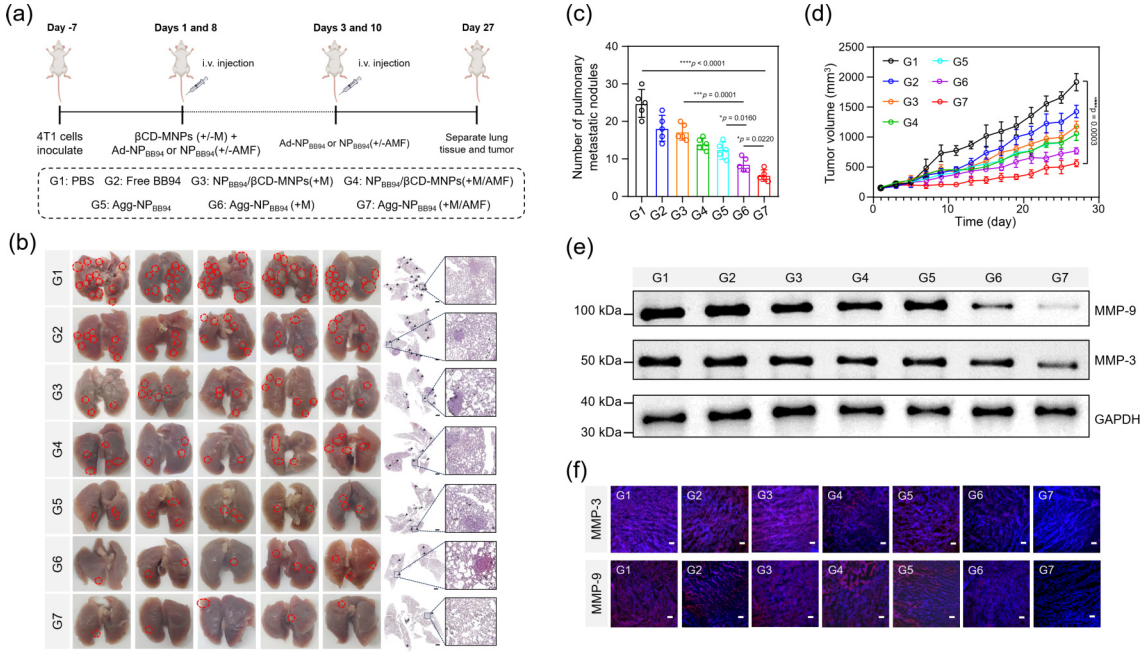

Figure 4 (a) Schematic illustrating of the experimental protocol for treatment in the 4T1 breast tumor model. (b) Images of lung tissues presented from mice after various treatments (n = 5). (c) Statistics of nodule numbers in lung tissues of *in situ* 4T1 tumor-bearing mice on day 27. Data are presented as the mean ± s.d. (n = 5). (d) The tumor growth curve of different mice groups with different treatments. Data are presented as the mean ± s.d. (n = 5). (e) Western blot analysis and (f) representative immunofluorescence staining images of MMP-3 and MMP-9 in mouse tumor tissues at the end of treatment. Scale bar, 60 μm.

randomly divided into four groups (n = 5): G1: PBS, G2: NP_{BMS-1}/βCD-MNPs(+M/AMF), G3: Agg-NP_{BMS-1}(+M), and G4: Agg-NP_{BMS-1}(+M/AMF). βCD-MNPs were first intravenously injected and magnetic-driven enrichment (+M) as described above together with a second injection of NP_{BMS-1} or Ad-NP_{BMS-1} at days 1, 5, and 9. Then, supplementary intravenous injections of NPBMS-1 or Ad-NPBMS-1 at a BMS-1 dosage of 5.0 mg/kg were administered, followed by the application of an alternating magnetic field (+AMF) on days 2, 6, and 10 (Fig. 5(a)). As shown in Fig. 5(b), the tumor inhibition rate of NP_{BMS-1}/βCD-MNPs(+M/AMF) was 34.2%, while it increased to 76.3% after receiving the Agg-NP_{BMS-1}(+M/AMF) treatment, achieving approximately 2.2-fold increase. And, the best therapeutic efficacy was further confirmed by collected tumor tissue at the end of therapy (Figs. 5(c) and 5(d)), and also exhibited good biosafety in the whole therapy period (Figs. 5(e) and 5(f)).

As described above, the BMS-1 would inhibit the PD-1/PD-L1 interaction, which could reactivate T cell-mediated antitumor immune responses. To demonstrate it, $CD8^+$ T cells and its subset were determined by flow cytometry. Figure 6(a) indicated that the proportions of $CD8^+$ T cells in NP_{BMS-1}/βCD-MNPs(+M/AMF) and Agg-NP_{BMS-1}(+M) group were elevated to 16.2% and 19.8%, respectively. And, the highest proportion of tumor-infiltrating $CD8^+$ T cells was observed in the Agg-NP_{BMS-1}(+M/AMF) group, reaching 33.3%. Moreover, its subset, IFN-γ^+ $CD8^+$ T cells with the IFN-γ secretion capacity, were also obviously increased (Fig. 6(b)) and more infiltrating $CD8^+$ T cells were observed by staining of tumor sections (Fig. 6(c)) in the Agg-NP_{BMS-1}(+M/AMF) group. Finally, enzyme-linked immunosorbent assay (ELISA) analysis indicated the increased secretion of cytokines TNF-α, IFN-γ, IL-12p70, and IL-6 (Figs. 6(d)–6(g)), further demonstrating that this nanoparticular aggregation strategy can significantly enhance antitumor immune responses of extracellular drug BMS-1.

To further demonstrate the mechanism of elicited potent anticancer immune response in Agg-NP_{BMS-1}(+M/AMF) group, the collected tumor tissues were employed for transcriptome analysis. A total of 14,379 transcripts were measured, of which 1578 up-regulated and 54 down-regulated genes (fold change ≥ 2 and P < 0.05) were determined between PBS and Agg-NP_{BMS-1}(+M/AMF) groups (Fig. 6(h)). More importantly, T cell activation-related genes (Fig. 6(i)) were clearly upregulated in the Agg-NP_{BMS-1}(+M/AMF) group.

3 Conclusions

In summary, we developed nanoparticular aggregation strategy for extracellular targeted drug delivery and cancer immunotherapy. The pre-administrated βCD-MNPs were efficiently accumulated in tumor tissue under magnetic actuation, and then further improved the infiltration of another nanoparticle Ad-NPs and achieved their micro-sized aggregation via the host–guest interaction. This aggregation strategy significantly enhanced the tumor accumulation and retention of drug delivery systems in tumor tissue for remarkably improving the therapeutic activity of extracellular-targeted drugs batimastat and BMS-1. Moreover, this nanoparticular aggregation strategy is also applicable for the delivery of other drugs, which do not require intracellular uptake and including those that are easily taken up by cells, such as doxorubicin and the photothermal agent IR780. By utilizing this aggregation approach, large particle clusters are formed at the tumor site, creating an "extracellular drug depot", enabled sustained drug release at the tumor location. This work offered a facile and rationally designed delivery strategy for extracellular drugs delivery.

4 Experimental

4.1 Materials

Iron(II) chloride tetrahydrate ($FeCl_2{\cdot}4H_2O$) (MFCD00149709) and

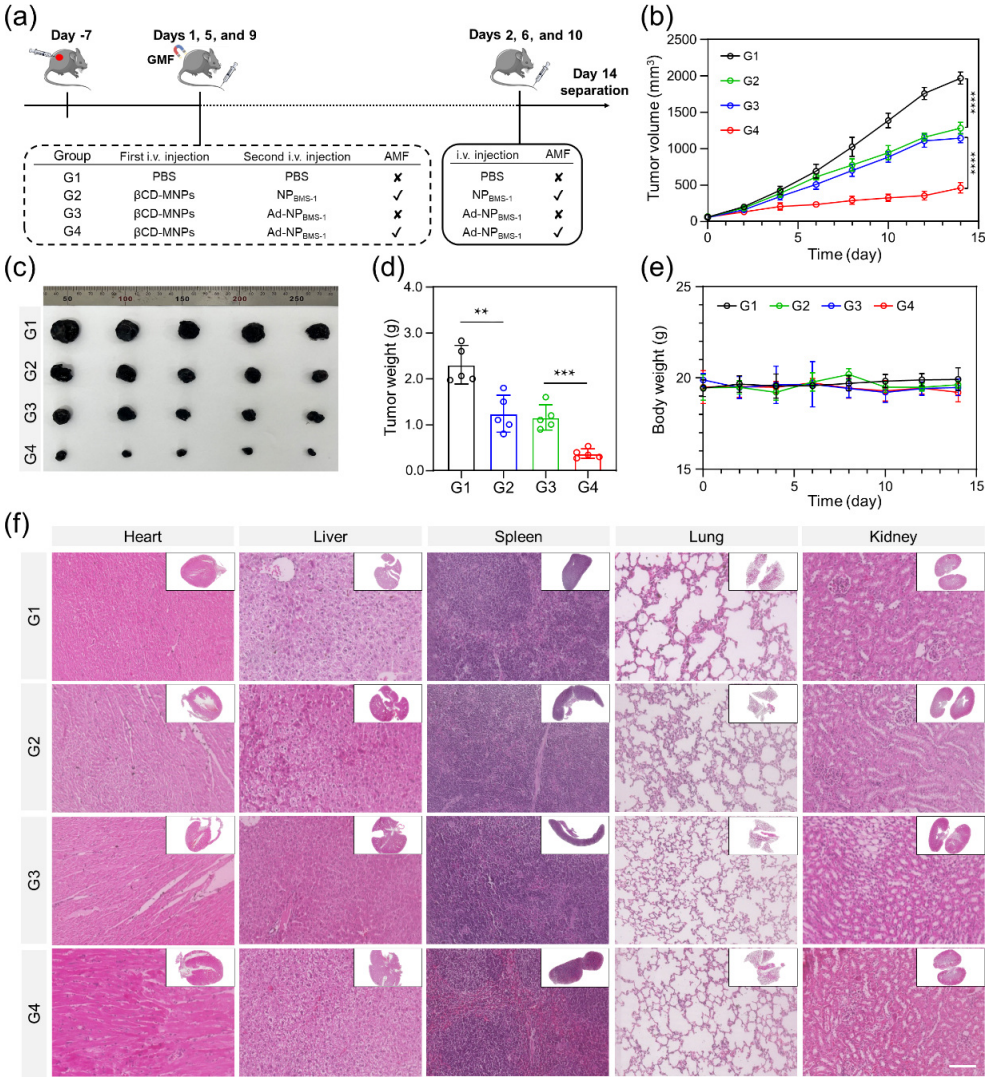

Figure 5 (a) Schematic illustrating of the experimental protocol for treatment in the B16-F10 melanoma tumor model. (b) The tumor growth curves of different mice groups with different treatments. Data are presented as the mean ± s.d. (n = 5). (c) The photograph and (d) weight of tumor tissues from different groups at the end of treatment. (e) The weight changes curve of mice at the therapy period from different groups. (f) H&E staining of main organs from treated-group mice. Scale bar, 50 μm.

carboxymethyl-β-cyclodextrin (MFCD00285608) were purchased from Macklin Biochemical Technology Co., Ltd. (Shanghai, China). Iron(III) chloride tetrahydrate ($FeCl_3·6H_2O$) (10011918) was purchased from Sinopharm Chemical Reagent Co., Ltd. (Shanghai, China). Amantadine hydrochloride (A1260) was purchased from Merck (Shanghai, China). Fluorescein isothiocyanate (FITC) (F4274), collagenase type IV, hyaluronidase (C4-BIOC), DNase I (11284932001), and DiD dye (468495) were purchased from Sigma-Aldrich (Missouri, USA). Dimethyl sulfoxide (DMSO) (300724008) was purchased from Sinopharm Chemical Reagent Co., Ltd. (Shanghai, China). BMS-1 was purchased from Apeptide Co., Ltd. (Shanghai, China). Batimastat (BB94) was purchased from Bide Pharmatech Ltd. (Shanghai, China). Hematoxylin and Eosin (H&E) (C0105S) staining kit was purchased from Beyotime (Shanghai, China). Bovine serum albumin (BSA) (4240GR025) was purchased from Suzhou Renold Biotechnology Co., Ltd. (Suzhou, China). FBS (209111) and centrifuge tubes (601001) were purchased from NEST Biotechnology Co. Ltd. (Wuxi, China). 4',6-Diamidino-2-phenylindole (DAPI) (62248) was purchased from Thermo Fisher Scientific (Shanghai, China). RPMI-1640 medium (10-040-CM), penicillin-streptomycin solution (100×) (30-002-CI), and trypsin (2.5%) (25-050-CI) were purchased from Corning Life Sciences Co., Ltd. (Suzhou, China). Anti-CD31 Rabbit pAb (GB11063-2-100) was purchased from Servicebio (Wuhan, China). HyperFluor™ 488 Goat Anti-Rabbit IgG (H+L) Antibody (K1206) was purchased from APExBIO (Houston, USA). TNF-α ELISA kit (JLW10484), IFN-γELISA kit (JLW10967) and IL-6 ELISA kit (JL20268) were purchased from Jianglai biology (Shanghai, China). IL-12p70 ELISA kit was purchased from Dakewe (Shenzhen, China). Flow cytometry antibodies and 10× red blood cell lysis solution (422401) were purchased from BioLegend (San Diego, USA).

4.2 Characterization

NMR spectra were recorded in deuterated reagent (such as DMSO-d6) with an NMR Bruker AVANCE III 400 MHz spectrometer (Bruker Scientific Corporation Ltd., Switzerland). The size measurement was carried out in aqueous solution using a Malvern ZS90 dynamic light scattering instrument (Malvern Instruments

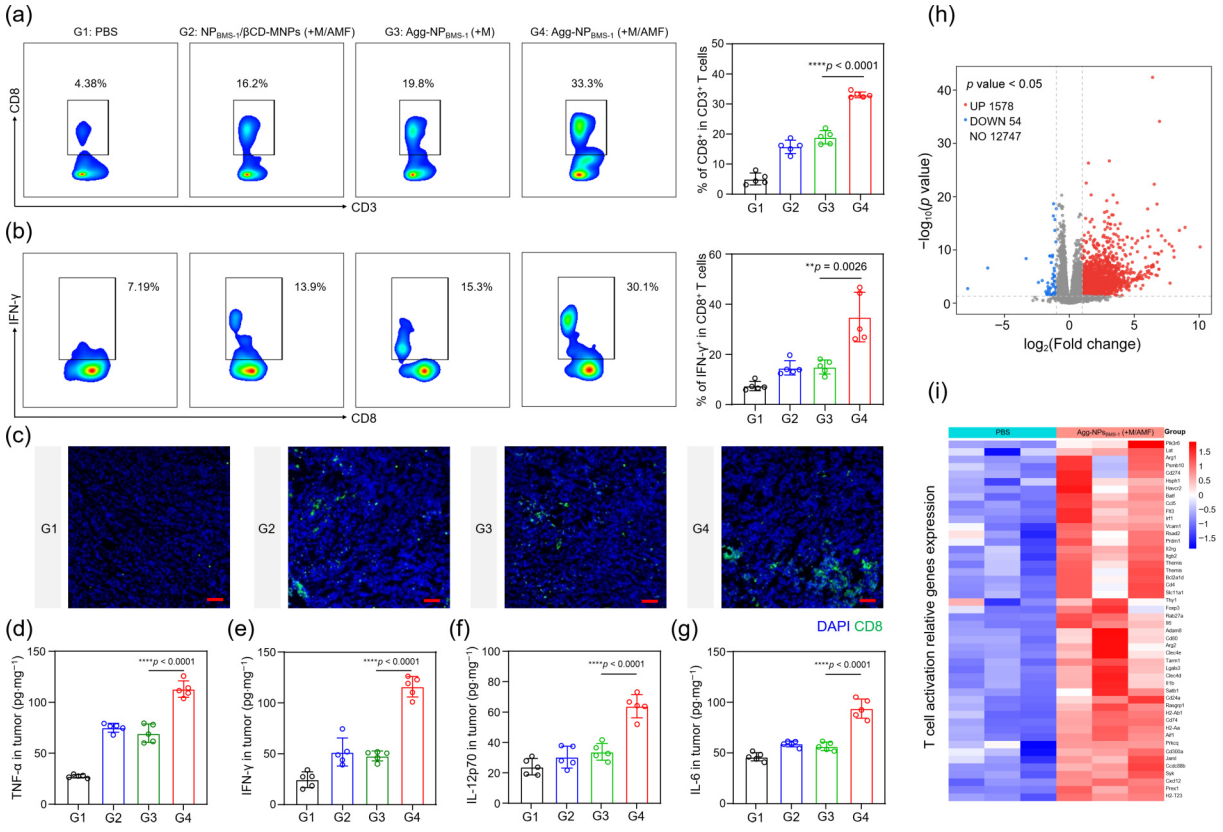

Figure 6 Representative flow cytometry images (left) and relative quantification (right) of (a) CD8$^+$ T cells and (b) IFN-γ$^+$ CD8$^+$ T cells (n = 5). (c) Images of infiltrating CD8$^+$ T cells staining in tumor section from various treatment groups. Scale bar, 50 μm. Levels of secreted (d) TNF-α, (e) IFN-γ, (f) IL-12p70, and (g) IL-6 in tumor tissues at the end of treatment (n = 5). (h) Distribution of upregulated (1578) and downregulated expression of genes (54) in the Agg-NPs$_{BMS-1}$(+M/AMF) group compared with the PBS group in a volcano plot. (i) Heat map of the T cell activation-related genes in the Agg-NPs$_{BMS-1}$(+M/AMF) group versus PBS group.

Ltd., England) with a He Ne laser (633 nm) and 90° collecting optics. The data were analyzed using Malvern Dispersion Technology Software 5.10. The fluorescence spectra were measured on a fluorescence spectrophotometer (Shimadzu RF 6000, Japan). The properties of the interaction between Ad-NPs and βCD-MNP were tested by isothermal titration calorimetry (nano ITC, USA) and atomic force microscopy (NanoWizard® 4 XP BioScience, USA).

4.3 Cell lines and animals

Murine breast cancer (4T1 cells) and mouse melanoma cells (B16-F10) were obtained from the American Type Culture Collection (ATCC). 4T1 cells and B16-F10 cells were cultured in RPMI-1640 medium supplemented with 10% FBS and 1% penicillin/streptomycin at 37 °C using a humidified 5% CO_2 incubator. Female BALB/c mice (6 weeks) were purchased from the Hunan SJA Laboratory Animal Co. Ltd. (Hunan, China). Mice were raised in Model Animal Center of South China University of Technology in a specific pathogen free (SPF) environment. All animals received care in compliance with the guidelines outlined in the Guide for the Care and Use of Laboratory Animals with free access to the feed and water. The animal study protocol was approved by the Institutional Animal Care and Use Committee at South China University of Technology with the assigned accreditation number 2022040.

4.4 Preparation of βCD-MNPs and Ad-NPs

$FeCl_2{\cdot}4H_2O$ (0.8 g) and $FeCl_3{\cdot}6H_2O$ (1.38 g) were mixed dissolved in 100 mL ultrapure water and stirred under vacuum circumstances. Subsequently, carboxymethyl-β-cyclodextrin (0.5 g) and NaOH (0.1 g/mL, 15 mL) were added and continuous mechanically stirred at 90 °C for 1 h. After cooling, the product solution was centrifuged (9000 rpm, 10 min) and washed three times with ultrapure water to obtain the magnetic nanoparticles, denoted as βCD-MNPs. The drug-encapsulated Ad-NPs were prepared according to a nanoprecipitation method. Simply, Ad-PEG-*b*-PLA (10 mg) and 1 mg batimastat (BB94) or BMS-1 were dissolved in 1 mL DMSO. After vortex, the mixed materials solution was dripped into 10 mL ultrapure water and kept stirring for 2 h at R.T. The obtained nanoparticles solution was transferred into a dialysis bag (MWCO = 14,000 Da) and put into ultrapure water for dialysis overnight. Then, the solution was collected inside the dialysis bag and concentrated by a YM 30 ultrafiltration centrifuge tube (Millipore, MWCO 5000 Da), and the obtained nanoparticles were denoted as Ad-NP$_{BB94}$ or Ad-NP$_{BMS-1}$. The control drug-loaded nanoparticles NP$_{BB94}$ or NP$_{BMS-1}$ were prepared according to similar method with PEG-*b*-PLA polymer. Furthermore, the drug loading capacity was determined by high performance liquid chromatography. The DiD-labeled Ad-NPs or NPs were prepared according to similar method with incorporating 1 wt.% DiD dye.

4.5 Aggregation of βCD-MNPs and Ad-NPs

In order to observe the crosslinking aggregate effect between βCD-MNPs and Ad-NPs, Ad-NP$_{DiD}$ (DiD dye-labeled, 1 mg/mL) and βCD-MNPs were mixed and co-incubated for different times. At different preset times, a magnet was placed at the bottom of the

tube to enrich the βCD-MNPs and the supernatant was collected to measure the fluorescence intensity of the supernatant by using a fluorescence spectrometer. After similar treatment based on DiD-labeled Ad-NPs (0.1 mg/mL) or NPs (0.1 mg/mL) and βCD-MNPs (0.1 mg/mL), the aggregates morphology of Agg-NPs was observed by three-dimensional (3D) CLSM. Moreover, βCD-MNPs (1 mg/mL) was co-incubated with Ad-NPs (1 mg/mL) or NPs for 1 min, respectively. The mixtures were then drop-cast onto adhesive glass slides and allowed to air dry naturally. The resulting morphology was subsequently examined using AFM.

4.6 Subject-object interaction force between βCD-MNPs and Ad-NPs or NPs

Ad-NPs (1 mg/mL) was loaded into the titration syringe, and βCD-MNPs (10 mg/mL) was placed in the sample cell. The thermal effects of Ad-NPs titration into βCD-MNPs were measured using an ITC. Additionally, βCD-MNPs were drop-cast onto adhesive glass slides, while the probe was immersed in Ad-NPs. After drying, the adhesive forces between particles were measured using AFM.

4.7 *In vivo* accumulation and crosslinking aggregate in tumor tissue of Agg-NPs

Mice were anesthetized and 4T1 cells (30 μL, 500,000 cells) were implanted into a vascular-rich region in the middle of the mouse ear. Tumor growth was monitored, and once the tumor reached approximately 50 mm^3, βCD-MNPs (10 mg/kg) were i.v. administered via tail in two groups of mice. After anesthetizing the mice, a magnet was placed over the ear tumor for 15 min. Subsequently, DiD-labeled Ad-NPs or NPs (1 mg/kg) were i.v. injected via tail vein, and particle accumulation was continuously observed for 110 min using CLSM (ZEISS990).

Furthermore, βCD-MNPs (10 mg/kg) were i.v. administered in each group of mice (n = 3), followed by the placement of a magnet at the tumor site for 15 min. Subsequently, DiD-labeled Ad-NPs or NPs (1 mg/kg) were i.v. injected, and the mice were subjected to an alternating magnetic field. The fluorescence intensity in the tumor regions was continuously monitored at 4, 12, 48, 96, 144, and 192 h by using an IVIS imaging system. Following IVIS imaging, tumor tissues were harvested and thoroughly ground using a steel mesh, and the resulting mixture was filtered through a nylon mesh to remove tissue debris. Finally, the residual fluorescence intensity of DiD in the tumor was quantified using a fluorescence spectrophotometer, and the concentration of residual Fe in the tumor tissue was analyzed using inductively coupled plasma mass spectrometry (ICP-MS).

4.8 Magnetothermal enhanced particles accumulation in tumor

To investigate the mechanism of magnetothermal-enhanced particle aggregation, the βCD-MNPs (10 mg/kg) were i.v. injection via tail into each mouse (n = 7 per group), followed by the placement of a magnet at the tumor site for 15 min. Subsequently, Ad-NPs (1 mg/kg) were i.v. injected. To simulate the heat effects induced by magnetothermal processes, βCD-MNPs were used as a photothermal agent, and an 808 nm laser was applied to irradiate the tumor site. Blood flow velocity in the tumor-surrounding vasculature was measured using a small animal ultrasound imaging system (VisualSonics Vevo® 2100 Imaging System). Additionally, tumor tissues, both subjected to magnetothermal treatment and untreated, were harvested and stained with H&E. The extent of tissue loosening within the tumor was analyzed using ImageJ software.

4.9 *In vivo* antitumor efficacy of Agg-NPs delivers BB94

Female BALB/c mice bearing 4T1 tumors (~ 50 mm^3) were randomly divided into 7 groups (n = 5 per group): G1: PBS, G2: free BB94, G3: NP_{BB94}/βCD-MNPs(+M), G4: NP_{BB94}/βCD-MNPs(+M/AMF), G5: Agg-NP_{BB94}, G6: Agg-NP_{BB94}(+M), and G7: Agg-NP_{BB94}(+M/AMF). On days 1 and 8, the following treatments were administered via intravenous injection: G1: PBS, G2: free BB94, and for groups G3, G4, G6, and G7, βCD-MNPs were injected followed by placing a magnet at the tumor site for 15 min, after which Ad-NP_{BB94} or NP_{BB94} was i.v. injected. G4 and G7 were additionally subjected to an alternating magnetic field. G5 was administrated similar as G7 but without placed magnet and alternating magnetic field. On days 3 and 10, the same treatments were repeated as abovementioned. The dosage of BB94 was 5 mg/kg. Tumor size and body weight were measured every two days. Tumor volume (mm^3) was calculated using the formula $V = L \times W^2 \times 1/2$, where L is the longest dimension and W is the shortest dimension. At the end of the treatment, the mice were sacrificed, tumor and lung tissues were collected from each group. The number of lung nodules was quantified, and lung tissues were subjected to H&E staining for histological analysis. Immunofluorescence staining was performed to assess the expression of MMP-3 and MMP-9 proteins in the tumor tissues. Additionally, tumor tissues were homogenized, and the expression levels of MMP-3 and MMP-9 proteins were further analyzed by western blot.

4.10 *In vivo* antitumor efficacy of Agg-NPs delivers BMS-1

Female C57BL/6j mice bearing B16-F10 tumors (~ 50 mm^3) were randomly divided into 4 groups (n = 5 per group): On days 1, 5, and 9, the following treatments were administered: G1: PBS, G2: $NP_{BMS\text{-}1}$/βCD-MNPs(+M/AMF), G3: Agg-$NP_{BMS\text{-}1}$(+M), G4: Agg-$NP_{BMS\text{-}1}$(+M/AMF). Groups G2, G3, and G4 were i.v. injected with βCD-MNPs, followed by placement of a magnet at the tumor site for 15 min at days 1, 5, and 9. Subsequently, $NP_{BMS\text{-}1}$ or Ad-$NP_{BMS\text{-}1}$ was i.v. injected and following application of an alternating magnetic field at days 2, 6, and 10. The dosage of BMS-1 was 5 mg/kg mice weight. Tumor size and body weight were recorded every two days. Tumor volume (mm^3) was calculated using the formula $V = L \times W^2 \times 1/2$, where L is the longest dimension and W is the shortest dimension. Tumor tissues were harvested and homogenized for flow cytometric analysis of immune cell levels, and tumor samples from G1 and G4 groups were sent for transcriptomic analysis. Finally, major organs from each group were collected and subjected to H&E staining for safety evaluation.

4.11 Analysis of immune effects

Tumors excised from mice were minced and incubated in a digestion solution at 37 °C for 15 min, and then cell suspensions were passed through a 200-mesh steel mesh, centrifuged and 40% percoll was added to isolate lymphocytes by gradient centrifugation. Next, red blood cell lysis buffer was added at room temperature for 10 min. Then, the samples were centrifuged and resuspended in PBS containing 0.2% bovine serum albumin. The extracted lymphocytes were collected and stained with Brilliant Violet 510™ anti-mouse CD45 (clone: 104), FITC anti-mouse CD3 (clone:

17A2), APC/Cyanine7 anti-mouse CD4 (clone: GK1.5), PE anti-mouse CD8a (clone: 56-6.7), and APC anti-mouse IFN-γ (clone: XMG1.2) for flow cytometry analysis.

4.12 Statistical analysis

All data were presented as the mean ± s.d. The results were analyzed using one-way ANOVA or unpaired two-sided Student's *t*-test with GraphPad Prism 8.0 (GraphPad Software). Values of $p < 0.05$ were considered to be statistically significant (*$p < 0.05$, **$p < 0.01$, ***$p < 0.001$, ****$p < 0.0001$, ns: no significance).

Data availability

All data needed to support the conclusions in the paper are presented in the manuscript and the Electronic Supplementary Material. Additional data related to this paper may be requested from the corresponding author upon request.

Electronic Supplementary Material: Supplementary material (characterization of βCD-MNPs and Ad-PEG-*b*-PLA, CLSM image of Agg-NSs, analysis of loose area and blood flow, image of tumor tissues, graph of weight changes and biochemical criterion) is available in the online version of this article at https://doi.org/10.26599/NR.2025.94907164.

Acknowledgements

This work was supported by the National Natural Science Foundation of China (Nos. 52425304, U22A20156, and 52173121), the Guangzhou Science and Technology Planning Project (No. 2024A03J1181), and the GuangDong Basic and Applied Basic Research Foundation (Nos. 2024A1515011130 and 2024B1515020106).

Declaration of competing interest

All the contributing authors report no conflict of interests in this work.

Author contributions statement

X. Z. Y., Z. Y. C., and F. Z. L. proposed the idea and designed the experiments. F. Z. L. performed the experiments. F. Z. L., Y. Q. Z., C. R. C., D. L. Q., and H. L., analyzed the data and provided valuable advice. All authors contributed to the writing of the manuscript, discussed the results and implications, and edited the manuscript at all stages.

Informed consent

Not applicable.

Ethics statement

The animal experiments were carried out following the guidelines of the South China University of Technology Animal Care and Use Committee (Ethical code: 2022040).

Use of AI statement

None.

References

[1] Mura, S.; Nicolas, J.; Couvreur, P. Stimuli-responsive nanocarriers for drug delivery. *Nat. Mater.* **2013**, *12*, 991–1003.
[2] Wu, J. Y.; Pu, K. Y. Leveraging semiconducting polymer nanoparticles for combination cancer immunotherapy. *Adv. Mater.* **2024**, *36*, 2308924.
[3] Yang, G.; Pan, X. X.; Feng, W. B.; Yao, Q. F.; Jiang, F. Y.; Du, F. L.; Zhou, X. F.; Xie, J. P.; Yuan, X. Engineering Au_{44} nanoclusters for NIR-II luminescence imaging-guided photoactivatable cancer immunotherapy. *ACS Nano* **2023**, *17*, 15605–15614.
[4] Huang, J.; Liu, X. L.; Lin, M. Z.; Xiao, Z. C.; & Shuai, X. T. Light-inducible nanodrug-mediated photodynamic and anti-apoptotic synergy for enhanced immunotherapy in triple-negative breast cancer. *Biomater. Sci.* **2024**, *12*, 2639–2647.
[5] Pang, X. R.; Fu, C. P.; Chen, J. B.; Su, M.; Wei, R. L.; Wang, Y.; Lin, W. X.; Wei, X. H.; Jiang, X. Q.; Yang, X. Z. et al. A manganese-phenolic network platform amplifying STING activation to potentiate MRI guided cancer chemo-/chemodynamic/immune therapy. *Biomater. Sci.* **2023**, *11*, 3840–3850.
[6] Yu, H.; Wang, Q.; Zhang, X. M.; Tiemuer, A.; Wang, J.; Zhang, Y. Y.; Sun, X. L.; Liu, Y. Hot-band absorption assisted single-photon frequency upconversion luminescent nanophotosensitizer for 808 nm light triggered photodynamic immunotherapy of cancer. *Biomater. Sci.* **2023**, *11*, 2167–2176.
[7] Wang, S.; Zhang, F. W.; Yu, G. C.; Wang, Z. T.; Jacobson, O.; Ma, Y.; Tian, R.; Deng, H. Z.; Yang, W. J.; Chen, Z. Y. et al. Zwitterionic-to-cationic charge conversion polyprodrug nanomedicine for enhanced drug delivery. *Theranostics* **2020**, *10*, 6629–6637.
[8] He, Y. J.; Su, Z. G.; Xue, L. J.; Xu, H.; Zhang, C. Co-delivery of erlotinib and doxorubicin by pH-sensitive charge conversion nanocarrier for synergistic therapy. *J. Control. Release* **2016**, *229*, 80–92.
[9] Du, J. Z.; Sun, T. M.; Song, W. J.; Wu, J.; Wang, J. A tumor-acidity-activated charge-conversional nanogel as an intelligent vehicle for promoted tumoral-cell uptake and drug delivery. *Angew. Chem., Int. Ed.* **2010**, *49*, 3621–3626.
[10] Zhu, Y. Q.; Song, Y. H.; Cao, Z. Y.; Dong, L.; Shen, S.; Lu, Y.; Yang, X. Z. A magnetically driven amoeba-like nanorobot for whole-process active drug transport. *Adv. Sci.* **2023**, *10*, 2204793.
[11] Yu, W. Q.; Liu, R.; Zhou, Y.; Gao, H. L. Size-tunable strategies for a tumor targeted drug delivery system. *ACS Cent. Sci.* **2020**, *6*, 100–116.
[12] Liang, M. Y.; Zhang, M. J.; Qiu, W.; Xiao, Y.; Ye, M. J.; Xue, P.; Kang, Y. J.; Sun, Z. J.; Xu, Z. G. Stepwise size shrinkage cascade-activated supramolecular prodrug boosts antitumor immunity by eliciting pyroptosis. *Adv. Sci.* **2022**, *9*, 2203353.
[13] Zhu, S. S.; Gao, H.; Li, W. Y.; He, X. C.; Jiang, P. P.; Xu, F.; Jin, G. R.; Guo, H. Stimuli-responsive aptamer-drug conjugates for targeted drug delivery and controlled drug release. *Adv. Healthc. Mater.* **2024**, *13*, 2401020.
[14] Wei, D. S.; Sun, Y.; Zhu, H.; Fu, Q. R. Stimuli-responsive polymer-based nanosystems for cancer theranostics. *ACS Nano* **2023**, *17*, 23223–23261.
[15] Ding, D. D.; Mei, Z. H.; Huang, H.; Feng, W.; Chen, L.; Chen, Y.; Zhou, J. Q. Oxygen-independent sulfate radical for stimuli-responsive tumor nanotherapy. *Adv. Sci.* **2022**, *9*, 2200974.
[16] Yan, X.; Li, K.; Xie, T. Q.; Jin, X. K.; Zhang, C.; Li, Q. R.; Feng, J.; Liu, C. J.; Zhang, X. Z. Bioorthogonal "click and release" reaction-triggered aggregation of gold nanoparticles combined with released lonidamine for enhanced cancer photothermal therapy. *Angew. Chem., Int. Ed.* **2024**, *63*, e202318539.
[17] Wilhelm, S.; Tavares, A. J.; Dai, Q.; Ohta, S.; Audet, J.; Dvorak, H. F.; Chan, W. C. W. Analysis of nanoparticle delivery to tumours. *Nat. Rev. Mater.* **2016**, *1*, 16014.
[18] Shi, J. J.; Kantoff, P. W.; Wooster, R.; Farokhzad, O. C. Cancer

nanomedicine: Progress, challenges and opportunities. *Nat. Rev. Cancer* **2017**, *17*, 20–37.

[19] Price, L. S. L.; Stern, S. T.; Deal, A. M.; Kabanov, A. V.; Zamboni, W. C. A reanalysis of nanoparticle tumor delivery using classical pharmacokinetic metrics. *Sci. Adv.* **2020**, *6*, eaay9249.

[20] Danhier, F. To exploit the tumor microenvironment: Since the EPR effect fails in the clinic, what is the future of nanomedicine. *J. Control. Release* **2016**, *244*, 108–121.

[21] You, Q. Y.; Hu, M. D.; Qian, H. Advanced nanoarchitectonics of drug delivery systems with pyroptosis inhibition for noncancerous disease treatment. *Adv. Funct. Mater.* **2024**, *34*, 2315199.

[22] Kudryavtseva, V.; Sukhorukov, G. B. Features of anisotropic drug delivery systems. *Adv. Mater.* **2024**, *36*, 2307675.

[23] Arévalo-Pérez, R.; Maderuelo, C.; Lanao, J. M. Recent advances in colon drug delivery systems. *J. Control. Release* **2020**, *327*, 703–724.

[24] Cao, Z. Y.; Li, D. D.; Zhao, L.; Liu, M. T.; Ma, P. Y.; Luo, Y. L.; Yang, X. Z. Bioorthogonal *in situ* assembly of nanomedicines as drug depots for extracellular drug delivery. *Nat. Commun.* **2022**, *13*, 2038.

[25] Zhang, Y.; Zhao, G.; Chen, Y. F.; Zhou, S. K.; Wang, Y.; Sun, Y. Q.; Shen, S.; Xu, C. F.; Wang, J. Engineering nano-clustered multivalent agonists to cross-link TNF receptors for cancer therapy. *Aggregate* **2023**, *4*, e393.

[26] Lao, X. Y.; Liu, Y.; Li, L. H.; Song, M. L.; Ma, Y. J.; Yang, M.; Chen, G. Y.; Hao, J. H. Plasmon-enhanced FRET biosensor based on Tm^{3+}/Er^{3+} co-doped core–shell upconversion nanoparticles for ultrasensitive virus detection. *Aggregate* **2024**, *5*, e448.

[27] Tang, S.; Meng, Q. S.; Sun, H. P.; Su, J. H.; Yin, Q.; Zhang, Z. W.; Yu, H. J.; Chen, L. L.; Chen, Y.; Gu, W. W. et al. Tumor-microenvironment-adaptive nanoparticles codeliver paclitaxel and siRNA to inhibit growth and lung metastasis of breast cancer. *Adv. Funct. Mater.* **2016**, *26*, 6033–6046.

[28] Li, K.; Tay, F. R.; Yiu, C. K. Y. The past, present and future perspectives of matrix metalloproteinase inhibitors. *Pharmacol. Ther.* **2020**, *207*, 107465.

[29] de Almeida, L. G. N.; Thode, H.; Eslambolchi, Y.; Chopra, S.; Young, D.; Gill, S.; Devel, L.; Dufour, A. Matrix metalloproteinases: From molecular mechanisms to physiology, pathophysiology, and pharmacology. *Pharmacol. Rev.* **2022**, *74*, 712–768.

[30] Sleeboom, J. J. F.; van Tienderen, G. S.; Schenke-Layland, K.; van der Laan, L. J. W.; Khalil, A. A.; Verstegen, M. M. A. The extracellular matrix as hallmark of cancer and metastasis: From biomechanics to therapeutic targets. *Sci. Transl. Med.* **2024**, *16*, eadg3840.

[31] Li, D.; Chen, X. H.; Dai, W. B.; Jin, Q.; Wang, D.; Ji, J.; Tang, B. Z. Photo-triggered cascade therapy: A NIR-II AIE luminogen collaborating with nitric oxide facilitates efficient collagen depletion for boosting pancreatic cancer phototheranostics. *Adv. Mater.* **2024**, *36*, 2306476.

[32] Wu, P. K.; Zhang, H. T.; Yin, Y.; Sun, M. L.; Mao, S.; Chen, H. H.; Deng, Y. X.; Chen, S.; Li, S.; Sun, B. C. Engineered EGCG-containing biomimetic nanoassemblies as effective delivery platform for enhanced cancer therapy. *Adv. Sci.* **2022**, *9*, 2105894.

[33] Chen, Q.; Wang, C.; Zhang, X. D.; Chen, G. J.; Hu, Q. Y.; Li, H. J.; Wang, J. Q.; Wen, D.; Zhang, Y. Q.; Lu, Y. F. et al. *In situ* sprayed bioresponsive immunotherapeutic gel for post-surgical cancer treatment. *Nat. Nanotechnol.* **2019**, *14*, 89–97.

[34] Xin, Q.; Wang, D. J.; Wang, S. H.; Zhang, L. R.; Liang, Q.; Yan, X. Y.; Fan, K. L.; Jiang, B. Tackling esophageal squamous cell carcinoma with ITFn-Pt(IV): A novel fusion of PD-L1 blockade, chemotherapy, and T-cell activation. *Adv. Healthc. Mater.* **2024**, *13*, 2303623.

[35] Wang, K. W.; Jiang, M. L.; Li, T.; Liu, Y.; Zong, Q. Y.; Xu, Q.; Ullah, I.; Chen, Y. H.; Xue, W.; Yuan, Y. Y. A synergistic chemoimmunotherapy system leveraging PD-L1 blocking and bioorthogonal prodrug activation. *Adv. Mater.* **2024**, *36*, 2402322.

[36] Liang, S.; Xiao, L. Y.; Chen, T.; Roa, P.; Cocco, E.; Peng, Z. W.; Yu, L.; Wu, M. Y.; Liu, J.; Zhao, X. Z. et al. Injectable nanocomposite hydrogels improve intraperitoneal co-delivery of chemotherapeutics and immune checkpoint inhibitors for enhanced peritoneal metastasis therapy. *ACS Nano* **2024**, *18*, 18963–18979.

[37] Cao, F. F.; Jin, L. L.; Gao, Y.; Ding, Y.; Wen, H. Y.; Qian, Z. F.; Zhang, C. Y.; Hong, L. J.; Yang, H.; Zhang, J. J. et al. Artificial-enzymes-armed *Bifidobacterium longum* probiotics for alleviating intestinal inflammation and microbiota dysbiosis. *Nat. Nanotechnol.* **2023**, *18*, 617–627.

[38] Yang, H.; Yang, S. S.; Guo, Q. S.; Sheng, J. F.; Mao, Z. W. ATP-responsive manganese-based bacterial materials synergistically activate the cGAS-STING pathway for tumor immunotherapy. *Adv. Mater.* **2024**, *36*, 2310189.

[39] Tizro, N.; Moniri, E.; Saeb, K.; Panahi, H. A.; Ardakani, S. S. Preparation and application of grafted β-cyclodextrin/thermo-sensitive polymer onto modified Fe_3O_4@SiO_2 nano-particles for fenitrothion elimination from aqueous solution. *Microchem. J.* **2019**, *145*, 59–67.

[40] Ke, Y.; Zhang, X. Y.; Liu, C. K.; Xiao, M.; Li, H.; Fan, J. C.; Fu, P. C.; Wang, S. H.; Zan, F.; Wu, G. Polypseudorotaxane functionalized magnetic nanoparticles as a dual responsive carrier for roxithromycin delivery. *Mater. Sci. Eng. C* **2019**, *99*, 159–170.

[41] Chen, X. H.; Wang, S.; Chen, Y. X.; Xin, H. H.; Zhang, S. S.; Wu, D.; Xue, Y. N.; Zha, M. L.; Li, H. J.; Li, K. et al. Non-invasive activation of intratumoural gene editing for improved adoptive T-cell therapy in solid tumours. *Nat. Nanotechnol.* **2023**, *18*, 933–944.

[42] Wang, Q.; Liang, Q. R.; Dou, J. X.; Zhou, H.; Zeng, C. C.; Pan, H. M.; Shen, Y. Q.; Li, Q.; Liu, Y.; Leong, D. T. et al. Breaking through the basement membrane barrier to improve nanotherapeutic delivery to tumours. *Nat. Nanotechnol.* **2024**, *19*, 95–105.

[43] Dong, W.; Li, Z. B.; Hou, T. L.; Shen, Y. Q.; Guo, Z. X.; Su, Y. T.; Chen, Z. Q.; Pan, H. M.; Jiang, W.; Wang, Y. C. Multicomponent synthesis of imidazole-based ionizable lipids for highly efficient and spleen-selective messenger RNA delivery. *J. Am. Chem. Soc.* **2024**, *146*, 15085–15095.

[44] Jiang, W.; Dong, W.; Li, M.; Guo, Z. X.; Wang, Q.; Liu, Y.; Bi, Y. H.; Zhou, H.; Wang, Y. C. Nitric oxide induces immunogenic cell death and potentiates cancer immunotherapy. *ACS Nano* **2022**, *16*, 3881–3894.

[45] Setyawati, M. I.; Wang, Q.; Ni, N. Y.; Tee, J. K.; Ariga, K.; Ke, P. C.; Ho, H. K.; Wang, Y. C.; Leong, D. T. Engineering tumoral vascular leakiness with gold nanoparticles. *Nat. Commun.* **2023**, *14*, 4269.

[46] Duhachek-Muggy, S.; Qi, Y.; Wise, R.; Alyahya, L.; Li, H.; Hodge, J.; Zolkiewska, A. Metalloprotease-disintegrin ADAM12 actively promotes the stem cell-like phenotype in claudin-low breast cancer. *Mol. Cancer* **2017**, *16*, 32.

[47] Yu, T.; Nie, W.; Hong, Z. H.; He, Y. H.; Chen, J.; Mi, X.; Yang, S. P.; Li, X. L.; Wang, B. L.; Lin, Y. Z. et al. Synergy of immunostimulatory genetherapy with immune checkpoint blockade motivates immune response to eliminate cancer. *Adv. Funct. Mater.* **2021**, *31*, 2100715.

[48] Yu, J.; Liu, S.; Wang, Y. P.; He, X. D.; Zhang, Q. F.; Qi, Y. X.; Zhou, D. F.; Xie, Z. G.; Li, X. Y.; Huang, Y. B. Synergistic enhancement of immunological responses triggered by hyperthermia sensitive Pt NPs via NIR laser to inhibit cancer relapse and metastasis. *Bioact. Mater.* **2022**, *7*, 389–400.

This is an open access article under the terms of the Creative Commons Attribution 4.0 International License (CC BY 4.0, https://creativecommons.org/licenses/by/4.0/).

© The Author(s) 2025. Published by Tsinghua University Press.